

Free vibration analysis of locally damaged aerospace tapered composite structures using component-wise models

Original

Free vibration analysis of locally damaged aerospace tapered composite structures using component-wise models / Viglietti, A.; Zappino, E.; Carrera, E.. - In: COMPOSITE STRUCTURES. - ISSN 0263-8223. - 192:(2018), pp. 38-51. [10.1016/j.compstruct.2018.02.054]

Availability:

This version is available at: 11583/2704001 since: 2018-03-22T09:50:55Z

Publisher:

Elsevier Ltd

Published

DOI:10.1016/j.compstruct.2018.02.054

Terms of use:

This article is made available under terms and conditions as specified in the corresponding bibliographic description in the repository

Publisher copyright

Elsevier postprint/Author's Accepted Manuscript

© 2018. This manuscript version is made available under the CC-BY-NC-ND 4.0 license
<http://creativecommons.org/licenses/by-nc-nd/4.0/>. The final authenticated version is available online at:
<http://dx.doi.org/10.1016/j.compstruct.2018.02.054>

(Article begins on next page)

Free vibration analysis of locally damaged aerospace tapered composite structures using component-wise models

A. Viglietti^a, E. Zappino^{a,b}, E. Carrera^a

^a*MUL² Group, Department of Mechanical and Aerospace Engineering, Politecnico di Torino*

^b*Corresponding Author, email: enrico.zappino@polito.it*

Abstract

This work presents the free vibration analysis of tapered aircraft structures made of composite and metallic materials, with reference to global and local damage. A refined one-dimensional model, developed in the framework of the Carrera Unified Formulation, has been used to provide a detailed description of structures. Multi-component aeronautical structures have been modeled adopting Lagrange polynomials to evaluate the displacement field over the cross-section. Each component has been described through the component-wise approach, with its own geometrical and mechanical characteristics. The effects of localized damage have been investigated, thanks to the accuracy of the layer-wise models adopted. The model has been assessed by comparing the results with classical FE models. The results show that the present approach provides an accurate solution for the free vibration analyses of complex structures and is able to predict the consequences of a global or local failure of a structural component. The computational efficiency and the accuracy of the model used in this work can be exploited to characterize the dynamic response of complex composite structures considering a large number of damage configurations.

Keywords: CUF, One-dimensional model, tapered beam, Composite material, Failure

1. Introduction

Aeronautical structures are composed of several components that distribute the loads they undergo. An increasing number of aeronautical parts are made of composite materials for weight saving purposes. It is clear that, given the multi-component nature of these kinds of structures, if one component fails, the stress distribution and the structural behavior changes according to the entity of the damage. The knowledge of these effects is a crucial point in the design process to increase the structural reliability and the safety factor. Moreover the timely damage detection of damage is important for maintenance programs. Several nondestructive tests, such as ultrasounds or the magnetic field test, already exist. However, an estimation of the location of

10 the damage is required to increase the efficiency of these methods. The presence of the damage
11 affects the dynamic response of a structure, and the variations in the frequencies and modal
12 shapes can be used to detect structural damage. Several works on this kind of damage detection
13 have been proposed. Zhang *et al.*[1] and Capozzucca [2] proposed analyses of damaged compos-
14 ite beams, studying vibration behavior. The work of Wang [3] used an FE method to detect
15 damage in wind turbine blades considering variations of the modal shape curvatures. Nguyen [4]
16 proposed a study on the detection of damage in which calculating the modal shapes were cal-
17 culated using three-dimensional beam elements. Pollayi and Yu [5] investigated the mechanical
18 behavior of a damaged rotor and wind turbines using beams, on the basis of the geometrically
19 nonlinear 3-D elasticity theory and the variational asymptotic beam sectional analysis (VABS).
20 Pérez et al. [6] adopted a different approach and performed extensive experimental analyses
21 on the vibration of damaged laminates. The presence of damage and the characteristics of the
22 damage can be estimated by referring to a database that includes information on the natural
23 frequencies and model shapes of a wide spectrum of damaged cases, using accurate measurements
24 of the real structure. This database can only be achieved through mathematical model analyses
25 because a great deal of experimental proofs is not recommended because of time and money con-
26 straints. These models should be able to provide very accurate displacement and strain/stress
27 fields. Damage introduces local and non-classical effects, which cannot always be detected by
28 the conventional FE models that are used in the aeronautic field. A three-dimensional analysis
29 is required to provide accurate results, but this can lead to huge computational costs. In this
30 work, an advanced beam model based on the Carrera Unified Formulation is proposed to deal
31 with damaged structures in order to obtain accurate results, but with low computational costs
32 expressed in terms of Degrees of Freedom (DOFs). Classical theories, such as the Euler-Bernoulli
33 beam model [7] or the Timoshenko beam model [8], are not suitable for damage detection. In
34 the last few years, many works have been proposed to extend the application of one-dimensional
35 models to any geometry, boundary condition or, mechanical complexity. In the aeronautical
36 field, for aerodynamic reasons, particular shapes such as tapered shape or twist angle, are used.
37 These factors increase the structural complexity and, as a result, more complex models are re-
38 quired. Tapered shapes are considered in this work. In this way, if the beam axis is placed in
39 the y-axis direction, the bending stiffness $EI(y)$ changes along the axis. The classical approxi-
40 mation introduced to deal with such geometries is a step-by-step approach, which involves the
41 subdivision of the structure into several rigidly prismatic beams with different cross-sections.
42 The approximation is improved by increasing the number of subdivisions. Analytical methods,

43 [8][9] are used to introduce the shear stress of a tapered beam. After the introduction of the FE
44 method, several works have been proposed. A modified stiffness matrix for tapered components
45 has been proposed by Just [10]. This work uses modified displacement functions which consider
46 the variations in the proprieties of the sections. Brown [11] presented a stiffness matrix formula-
47 tion for a linearly tapered beam, while Schreyer [12] proposed a beam theory for tapered beams,
48 in which the shear strain is considered. Many works have been proposed about aeronautical struc-
49 tures in the framework of the Carrera Unified Formulation. In the present 1-D CUF model, the
50 displacement field over the cross-section is described through expansion functions. This feature
51 allows the model to deal with arbitrary geometries, materials, and boundary conditions. After
52 the first models, which were based on Taylor expansions, Lagrange polynomials were introduced.
53 In this way, multi-component structures can be modeled through *ad-hoc* formulations of each
54 component (Component-Wise approach) [13]. Some of the works about this approach and its
55 capability in the aerospace field are those of [14][15] and [16]. The work of [17] deals, through the
56 CW approach, with different prismatic structures made of an isotropic material; several several
57 types of damage were considered. The frequencies were evaluated for each case and the modal
58 shapes were compared using MAC (Modal Assurance Criterion)[18]. This criterion has already
59 been employed in the civil field (damaged bridges) by Salawu and Williams [19]. The extension
60 of the models to tapered structures has been proposed in [20] and [21].

61 In this work some aircraft structures with a tapered shape are analyzed using a 1-D CUF
62 model, considering different types of damage. The paper is organized as follows. A first part
63 concerns the one-dimensional model: the theory, finite element solution and model of the damage
64 are presented. Subsequently, several results are discussed and, finally, the main remarks are
65 presented.

66 **2. Refined one-dimensional models formulation**

67 The damage detection through free vibration analyses requires models with three-dimensional
68 capabilities able able to deal with complex local phenomena. Here, the Carrera Unified Formu-
69 lation is presented to develop a one-dimensional refined model able to deal with this topic. After
70 some preliminaries, the basis and the advantages of the CUF are presented in this section, finally,
71 the damage modeling approach is introduced.

72 *Preliminaries*

73 At first, it's necessary to define the work space of this formulation. Two frames are used to
 74 achieve the model of a structure. The first frame (x_G, y_G, z_G) is the global coordinate system of
 75 the three-dimensional space. The beams formulation is derived at the local level, respect a second
 76 frame (x, y, z) . y is the local beam axis and x, z represent the plane of the beam cross-section.
 77 The beam model derived at the local level can be arbitrary placed in the space using rotations
 78 and translations. These frames are shown in Figure 1a.

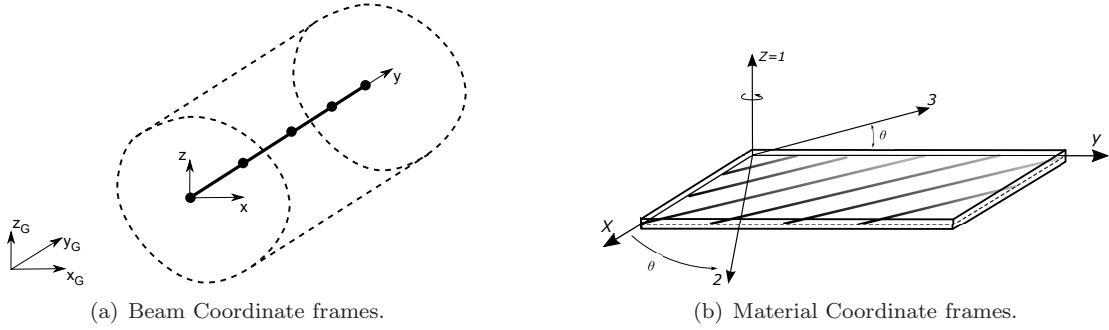


Figure 1: Reference frames.

79 The reference system $(1, 2, 3)$ is the material reference system. The local displacement vector
 80 is expressed as:

$$\mathbf{u}^T(x, y, z) = \{u_x \ u_y \ u_z\} \quad (1)$$

81 The stress vector $\boldsymbol{\sigma}$ and the strain one $\boldsymbol{\epsilon}$ are achieved as:

$$\boldsymbol{\sigma}^T(x, y, z) = \{\sigma_{xx}, \sigma_{yy}, \sigma_{zz}, \tau_{xy}, \tau_{xz}, \tau_{yz}\} \quad (2)$$

$$\boldsymbol{\epsilon}^T(x, y, z) = \{\epsilon_{xx}, \epsilon_{yy}, \epsilon_{zz}, \epsilon_{xy}, \epsilon_{xz}, \epsilon_{yz}\} \quad (3)$$

82 The strain vector is defined with the following linear strain-displacement relation:

$$\boldsymbol{\epsilon} = \mathbf{b}\mathbf{u} \quad (4)$$

83 where \mathbf{b} is a differential operator (a 6×3 matrix). The components of this matrix can be
 84 found in the book by Carrera *et al.* [22].

85 Hook's law provides the stress vector defined with the following equation:

$$\boldsymbol{\sigma} = \mathbf{C}\boldsymbol{\epsilon} \quad (5)$$

86 where \mathbf{C} is the 6×6 material coefficient matrix. It's a symmetric matrix, then $C_{ij} = C_{ji}$.
 87 \mathbf{C} changes the components respect the kind of considered material. A *anisotropic* material
 88 which has a different behavior in any direction, is composed of 21 independent coefficients.
 89 Instead, if the proprieties are the same along three perpendicular planes, the material is defined
 90 as *orthotropic* material and the coefficients become nine components. In this case, the matrix \mathbf{C}
 91 is defined as:

$$\mathbf{C} = \begin{bmatrix} C_{11} & C_{12} & C_{13} & 0 & 0 & 0 \\ C_{21} & C_{22} & C_{23} & 0 & 0 & 0 \\ C_{31} & C_{32} & C_{33} & 0 & 0 & 0 \\ 0 & 0 & 0 & C_{44} & 0 & 0 \\ 0 & 0 & 0 & 0 & C_{55} & 0 \\ 0 & 0 & 0 & 0 & 0 & C_{66} \end{bmatrix} \quad (6)$$

92 The matrix are composed by 12 terms, but due to the symmetry of the matrix, $C_{12} = C_{21}$,
 93 $C_{13} = C_{31}$ and $C_{23} = C_{32}$. For this reason the matrix is reduced to 9 components. With this
 94 type of material, the preferential direction of the material should be defined. For this reason,
 95 a third reference system is introduced referred to the material. This frame is figured in 1b.
 96 An example of an orthotropic material is a fiber-reinforced layer. This layer lies on the plane
 97 23 which is parallel to the plane xy . The axis 1 is aligned with the z -axis. Considering the
 98 axis 3 as the fiber direction, this one can be rotated with an angle of θ respect the y -axis. A
 99 positive counterclockwise rotation is considered. The present formulation allows the material
 100 to be oriented in an arbitrary direction to achieve particular lamination. As a consequence the
 101 transformation matrix \mathbf{T} is introduced:

$$\mathbf{C} = \begin{bmatrix} \cos^2\theta & \sin^2\theta & 0 & 0 & 0 & \sin 2\theta \\ \sin^2\theta & \cos^2\theta & 0 & 0 & 0 & -\sin 2\theta \\ 0 & 0 & 1 & 0 & 0 & 0 \\ 0 & 0 & 0 & \cos\theta & -\sin\theta & 0 \\ 0 & 0 & 0 & \sin\theta & \cos\theta & 0 \\ -\cos\theta\sin\theta & \cos\theta\sin\theta & 0 & 0 & 0 & \cos^2\theta - \sin^2\theta \end{bmatrix} \quad (7)$$

102 A *transformed material stiffness matrix* is introduced and it is expressed with the following
 103 form

$$\tilde{\mathbf{C}} = \mathbf{T}\mathbf{C}\mathbf{T}^T \quad (8)$$

104 This is the new stiffness matrix to be introduced in the Hooke's law.

$$\boldsymbol{\sigma} = \tilde{\mathbf{C}}\boldsymbol{\epsilon} \quad (9)$$

105 If the material has the same behavior in all directions, it is a *isotropic* material. Over any
 106 direction, the material provides the same behavior. In this case, there is no need to define
 107 a material reference system and a rotation matrix. The performance of the material can be
 108 described with only one value of the Poisson ratio and of Young's modulus. These assumptions
 109 lead to have

$$C_{11} = C_{22} = C_{33} \quad C_{12} = C_{13} = C_{23} \quad C_{44} = C_{55} = C_{66} \quad (10)$$

110 The explicit forms of \mathbf{C} terms can be found in the books by Tsai [23] or Reddy [24].

111 *Cross-sectional approximation*

112 The 1-D Carrera Unified Formulation (CUF) introduces the displacement field \mathbf{u} as the
 113 product of two contributions, one over the cross-section and one along the beam axis:

$$\mathbf{u}(x, y, z) = F_\tau(x, z)\mathbf{u}_\tau(y), \quad \tau = 1, 2 \dots M, \quad (11)$$

114 where \mathbf{u}_τ is the displacement vector, F_τ represents an expansion used to approximate the
 115 behavior of the beam cross-section and M is the number of the expansion terms. Depending on
 116 the used expansion, different classes of CUF model have been developed in the year, and two
 117 main classes have emerged. A first class uses the Taylor expansion as $F_\tau(x, z)$. Considering the
 118 TE model (TE: Taylor expansion) of the first order, the displacement field of the term u_x , for
 119 example, is expressed as follow:

$$u_x = u_{x_1} + xu_{x_2} + zu_{x_3} \quad (12)$$

120 The TE models can be deepened in [25]. The second class of CUF model uses the Lagrange
 121 polynomials to describe the cross-section through high-order elements. These model, using an

122 isoparametric formulation, allow us to built different multi-node elements in the natural domains.
 123 In this way, the model can describe the cross-section geometry without introducing approxima-
 124 tions in the real domain. The model used in this paper employs this expansion. Several sets of
 125 Lagrange polynomial exist, but in this work, in order to improve the accuracy, the nine-point set
 126 (L9) have been adopted. Other sets are for example L4 elements or L3 elements. More detail
 127 can be found in [26]. These functions, introducing as unknowns only translational displacements,
 128 have the following forms:

$$\begin{aligned}
 F_\tau &= \frac{1}{4}(r^2 + r * r_\tau)(s^2 + ss^\tau) & \tau = 1, 3, 5, 7 \\
 F_\tau &= \frac{1}{2}s^2_\tau(s^2 + ss_\tau)(1 - r^2) + \frac{1}{2}r^2_\tau((r^2 - rr_\tau)(1 - s^2) & \tau = 2, 4, 6, 8 \\
 F_\tau &= (1 - r^2)(1 - s^2) & \tau = 9
 \end{aligned}
 \tag{13}$$

129 where r and s can be a value between -1 and $+1$ and r_τ and s_τ are the coordinates of the nine
 130 points in the natural coordinate frame. In this way, considering the L9 element, the formulation
 131 of the displacement becomes:

$$\begin{aligned}
 u_x &= F_1u_{x_1} + F_2u_{x_2} + F_3u_{x_3} \dots + F_9u_{x_9} \\
 u_y &= F_1u_{y_1} + F_2u_{y_2} + F_3u_{y_3} \dots + F_9u_{y_9} \\
 u_z &= F_1u_{z_1} + F_2u_{z_2} + F_3u_{z_3} \dots + F_9u_{z_9}
 \end{aligned}
 \tag{14}$$

132 where $u_{x_{b1}} \dots u_{x_{b9}}$ represent the components x of the displacement field of each node of the
 133 L9 element.

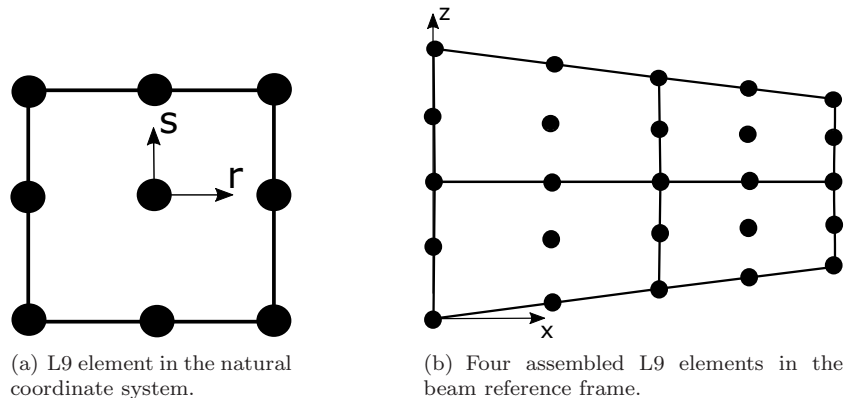


Figure 2: L9 elements.

134 Figure 2 shows on the left the L9 element in the natural reference system. Carrera and Petrolo
 135 [27] has demonstrated as the accuracy can be increased by using several L-elements in order to
 136 have a better refinement of the cross-section. The L-elements can be assembled as indicated on
 137 the right of figure 2.

138 *Finite Element formulation*

139 In order to solve the one-dimensional problem, the Finite Element model is used. The shape
 140 functions N_i are introduced to approximate the displacement over the beam axis (y) and then
 141 the vector \mathbf{u} can be written as

$$\mathbf{u}(x, y, z) = F_\tau(x, z)N_i(y)\mathbf{q}_{\tau i} \quad (15)$$

142 where $\mathbf{q}_{\tau i}$ is the nodal displacements vector.

143 The B3 elements (elements with three nodes) are adopted in this work and the index i
 144 indicates the node of the beam element. The shape functions can be arbitrarily chosen; the
 145 shape functions used in this work are reported in [22].

146 The governing equations can be obtained using the PVD (Principle of Virtual Displacements).
 147 The term δ denotes the virtual variation.

$$\delta L_{int} = -\delta L_{ine} \quad (16)$$

148 The two members of 16 are respectively the variation of the strain energy and the variation
 149 of the work performed by the inertial loads. The internal work can be written as follow:

$$\delta L_{int} = \int_V \delta \boldsymbol{\epsilon}^T \boldsymbol{\sigma} dV \quad (17)$$

150 The terms showed in 17 are already known. Expanding the inertial work the following form
 151 is obtained:

$$\delta L_{ine} = \int_V \delta \mathbf{u}^T \rho \ddot{\mathbf{u}} dV \quad (18)$$

152 where ρ is the density of the material and $\ddot{\mathbf{u}}$ is the acceleration vector.

153 From 17 and 18 the stiffness matrix \mathbf{K} and the mass matrix \mathbf{M} are achieved in terms of
 154 *fundamental nucleus (FN)*, a 3x3 block with fixed form. Its components are reported in [17]. A

155 complete description of the FN derivation and its use to achieve the global matrices are presented
 156 in [22].

157 For the sake of clarity, the form of the stiffness FN is now presented. Introducing the Hooke's
 158 law and the geometrical relations, the internal work can be expressed in function of the shape
 159 functions, the expansion used for the cross-section and the properties of the material.

$$\delta L_{int} = \delta \mathbf{q}_s^T \int_V N_j(y) F_s(x, z) \mathbf{b}^T \mathbf{C} \mathbf{b} F_\tau(x, z) N_i(y) dV \mathbf{q}_{\tau i} \quad (19)$$

160 The integral is the stiffness FN $\mathbf{k}^{ij\tau s}$. Each term of the fundamental nucleus has a fixed form.
 161 Equation 20 shows the extended formulation of two terms of the fundamental nucleus. The other
 162 terms can be obtained by the permutation of the indexes. The global stiffness matrix can be
 163 achieved varying the indexes i, j, τ and s .

$$\begin{aligned} k_{xx}^{\tau s ij} &= (\lambda + 2G) \int_l N_i N_j dy \int_A F_{\tau, x} F_{s, x} dA + G \int_l N_i N_j dy \int_A F_{\tau, z} F_{s, z} dA \\ &\quad + G \int_l N_{i, y} N_{j, y} dy \int_A F_\tau F_s dA; \\ k_{xy}^{\tau s ij} &= \lambda \int_l N_{i, y} N_{j, y} dy \int_A F_\tau F_{s, x} dA + G \int_l N_i N_j dy \int_A F_{\tau, x} F_s dA; \end{aligned} \quad (20)$$

164 Each beam can be arbitrary oriented in the space, the rotations and translation can be applied
 165 at each fundamental nucleus, as shown in [28], in order to write the global matrices in the global
 166 reference system. In this way, by imposing the congruence of the displacements in some nodes
 167 defined by the geometry, a complex structure can be obtained. More details can be found in [28]
 168 where the assembly procedure has been also described.

169 Knowing the form of \mathbf{K} and \mathbf{M} , the 16 can be rewritten as follows:

$$\mathbf{M} \ddot{\mathbf{u}} + \mathbf{K} \mathbf{u} = 0 \quad (21)$$

170 This is the undamped dynamic problem. Considering harmonic solutions and using the
 171 classical eigenvalue problem, the natural frequencies ω_k can be obtained.

$$(-\omega_k^2 \mathbf{M} + \mathbf{K}) \mathbf{u}_k = 0 \quad (22)$$

172 where \mathbf{u}_k is the k th eigenvector.

173 *Damage model description*

174 In this work the damage has been introduced through a degradation of the material properties
175 in a localized area. The following formulation has been used:

$$E_d = d \times E, \quad \text{with} \quad 0 \leq d \leq 1 \quad (23)$$

176 where E is Young's modulus of the undamaged material. E_d is the modulus of the deteriorated
177 material while d is the damage level. For $d = 1$ the material is undamaged while for $d = 0$ the
178 material is completely damaged, intermediate values can be used. Considering an orthotropic
179 material, the terms $E_{22}, E_{33}, G_{12}, \text{etc}$, are degraded in the same way. Thanks to the capabilities
180 of the present model, the damage can be introduced in the problem at different levels, as shown
181 in Figure 3. Considering a tapered panel with two stringers the damage can be introduced at the
182 component level, as in the case of a damaged stringer. Otherwise the damage can be introduced
183 at the layer level, as in the case in which just one layer collapses or, eventually, the damage can
184 be reduced only in a local area. In this case the degradation of the material has been included
185 locally. This approach can reproduce the situation in which just a small part of the structure is
186 damaged as in the case of local impacts. These concepts are more clear through the picture 3
187 which represents the damage.

188 **3. Numerical Results**

189 The following results refer to all the damage situations that can be investigated using the
190 present model: a component failure, a layer failure and local damage. Moreover, a complex
191 structure has been investigated to demonstrate the capabilities of the present approach in the
192 analysis of real configurations.

193 *3.1. Three stringer reinforced panel*

194 The reinforced structure shown in Figure 4a is considered. There are two panels with different
195 tapered shapes, which are reinforced by three square cross-section stringers. The panels are made
196 of a composite laminate, which has 4 layers lamination of $0^\circ/90^\circ/90^\circ/0^\circ$. The longitudinal axis
197 of the material, in the case of $\theta = 0^\circ$, coincides with the y_G axis. The composite material
198 is a *CFRP: Carbon Fiber Reinforced Polymer* with the following proprieties: $E_{LL} = 50 \text{ GPa}$,
199 $E_{TT} = E_{ZZ} = 10 \text{ GPa}$, $G = 5 \text{ GPa}$, Poissons's ratio $\nu = 0.25$ and density of 1700 kg/m^3 . E_{LL}
200 refers to the fiber direction. The reinforcements are made of an aluminum alloy. The Young

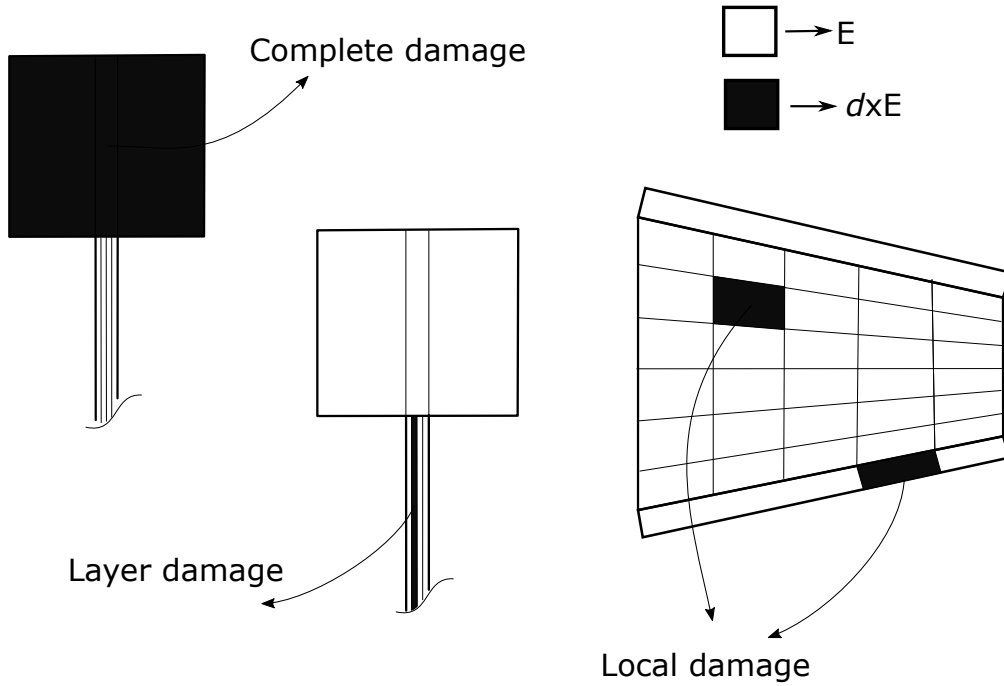


Figure 3: Different damage configurations: at a component level (stringer), at a layer level and at a local level.

201 Modulus is equal to $E = 71.7 \text{ GPa}$ and ν is equal to 0.3. The alloy has a density of 2810 kg/m^3 .
 202 The dimensions of the structures are: $L = 2$, $h_1 = 0.48$, $h_2 = 0.98$, $h_3 = 0.2$ and $h_4 = 0.4$. All
 203 the dimensions are expressed in meters. The stringers have a square cross-section with an area
 204 equal to 0.0016 m^2 . The central stiffener is parallel to the y_G axis.

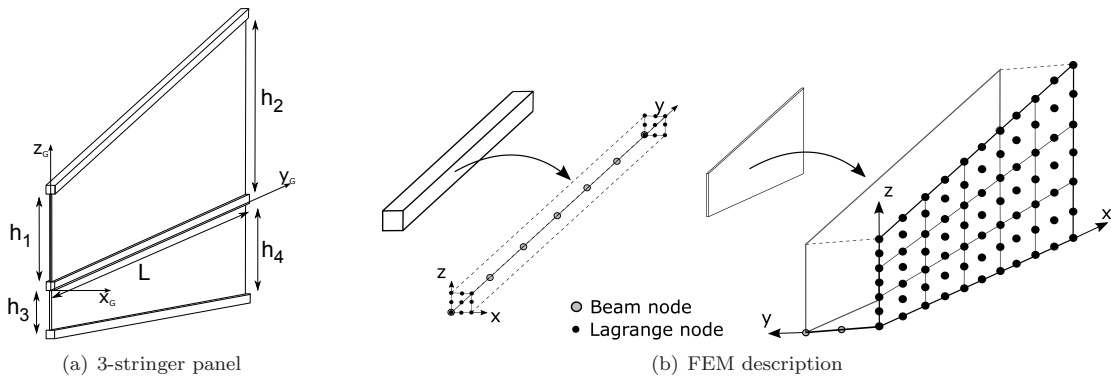


Figure 4: Three stringer reinforced panel: model description.

205 The reinforcements are described with six 4-node beam elements placed along the length of
 206 the component, and the square cross-section is described with three L9 elements.

207 The panel is described using 3-node beam elements over the thickness of each layer. The
208 tapered shape of the panel (the cross-section of the local beam) is made up of L9 elements (9×5
209 for the top panel and 9×4 for the bottom one). Figure 4b shows the details of the model. The
210 panel is represented by a cross-sectional mesh of 5×3 L9 elements. More details about this
211 approach used to describe composite panels can be found in [20] and [21].

212 3.2. Undamaged Panel

213 The undamaged panel has been investigated to assess of the model. The results have been
214 compared with those obtained using different models built using the commercial Nastran code.
215 The first model is a solid one (3D), while the second one uses shell elements for the panels and
216 beams for the stringers (1D-2D). Table 1 shows the first 15 frequencies obtained for the different
217 models. The first six columns report the classical theories and TE CUF Models. A step-modeling
218 approach was used for these models to approximate the tapered shape. Twenty beam elements
219 were adopted to discretize the structure. The solid model, which can be considered as the
220 reference model, was built using HEX8 solid elements. This approach leads to the very high
221 number of degrees of freedom, even when only one element is used through the thickness of each
222 lamina The component-wise model which is based on a Lagrange polynomial expansion (the LE
223 Model) is reported in the eighth column.

224 Classical theories are only able to identify the first frequency that is the first bending mode.
225 TE 3^{ed} and 4th order models can detect the first two bending modes, but they fail to consider
226 shell-like behavior. The LE model provides comparable frequencies with those of the
227 3D Nastran model. Figure 6a presents a comparison of the modal shapes for the present LE
228 model and the solid model. The MAC (Modal Assurance Criterion) was used to correlate the
229 modal shapes that were obtained using different models. MAC values equal to 1 mean that the
230 two analyzed modal shapes correspond. The picture shows that the current LE model is able
231 to detect all of the first 15 modes with a good correlation value if compared with the modes
232 obtained using the solid model.

233 The Nastran 1D-2D model was also considered since this modeling approach is widely used
234 in the aeronautical field. Sensible errors emerged, with respect to the the reference 3D values.
235 The related MAC graph shows the difficulty this model has in detecting the modal shapes at
236 higher frequencies. These differences are due to the approximations introduced to the connections
237 between the stringer and the panel. This phenomenon was discussed in detail in the work by
238 Cavallo *et al.*[29]. Figure 5 shows the first ten modal shapes of the studied structure.

DOF's	EBBT	TBT	Taylor step-wise models				LE model	Nastran Models	
			N=1	N=2	N=3	N=4		1D-2D	3D
	63	105	189	379	630	945	13167	38300	179700
f_1	8,63	8,63	8,63	7,83	7,61	7,52	7,14	7,08	7,14
f_2	53,46	53,46	53,46	30,42	29,09	28,11	7,89	7,83	7,96
f_3	150,29	150,29	150,29	48,57	47,18	46,49	12,31	11,51	13,58
f_4	274,84	274,84	274,78	98,01	91,47	86,20	13,02	12,58	14,53
f_5	298,15	298,15	298,15	136,84	132,82	127,89	18,02	16,57	20,49
f_6	501,70	501,70	490,30	204,73	185,90	135,12	23,75	21,67	26,62
f_7	679,45	679,45	501,70	254,51	188,72	175,55	28,44	25,7	30,26
f_8	766,74	766,74	603,79	271,89	241,32	202,38	32,54	26,98	32,99
f_9	785,99	785,99	785,26	361,31	262,50	233,22	36,07	31,67	38,43
f_{10}	1100,92	1100,92	766,73	458,16	296,29	257,21	41,33	34,7	42,35
f_{11}	1496,35	1496,35	1100,89	575,28	328,73	307,68	46,97	41,06	46,73
f_{12}	1513,93	1513,93	1181,44	588,61	426,39	370,59	47,57	43,28	47,80
f_{13}	1713,54	1713,54	1494,67	602,32	447,16	425,21	49,62	45,28	50,10
f_{14}	2017,58	2017,58	1513,87	702,43	522,09	490,40	50,85	46,43	50,85
f_{15}	2018,81	2018,81	1736,34	727,94	585,97	541,10	52,98	48,92	54,18

Table 1: First 15 frequencies of the 3-stringer composite panel obtained using different models.

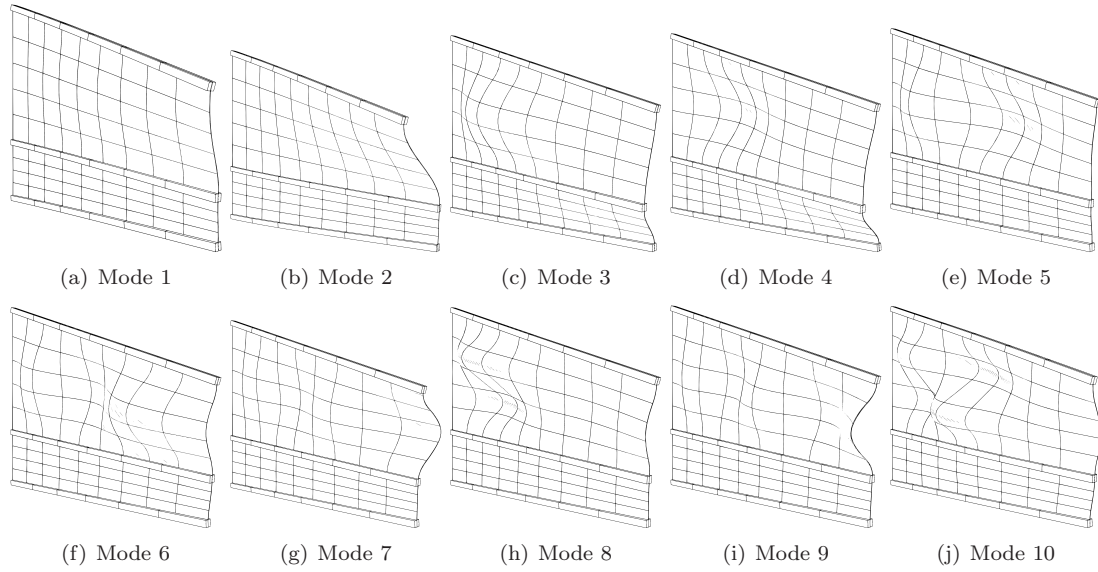


Figure 5: First 10 modal shapes evaluated using the LE model.

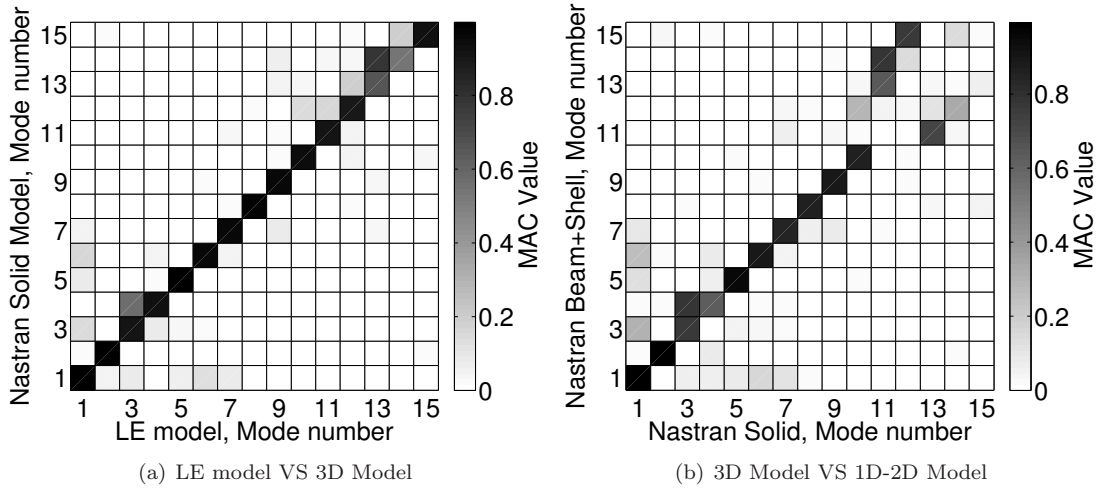


Figure 6: Correlation of the modal shapes of the undamaged structure evaluated using different models.

239 In conclusion the present assessment shows that the here adopted LE model is able to provide
 240 a comparable accuracy with that of solid models, with a marked reduction in the computational
 241 costs. Therefore, the present LE model has been used in the following sections to investigate
 242 damaged structures.

243 3.3. Damaged Panel

244 In this section, several types of damage have been considered. The first part concerns a
 245 component that is completely damaged. First the upper reinforcement was considered damaged.
 246 The free-vibration characteristics were evaluated and compared with those of the undamaged
 247 case. Then, the same process was applied to the top panel, the central stiffener and the bottom
 248 panel, one by one. These damage cases are presented in Figure 7. In the second part, the damage
 249 was considered at the layer level. An external and an internal layer were considered damaged in
 250 order to evaluate the worst case. Local damage was therefore introduced and the effects due to
 251 its position were investigated. Three different levels of degradation, d , were considered for each
 252 damage case: $d = 0.9$, $d = 0.5$ and $d = 0.1$. In the last case, the damaged components only had
 253 the 10% of the original stiffness.

254 3.3.1. Stiffened panel with a damaged component

255 In this section, the damage has been considered at the component level. Figure 7 shows the
 256 four considered cases.

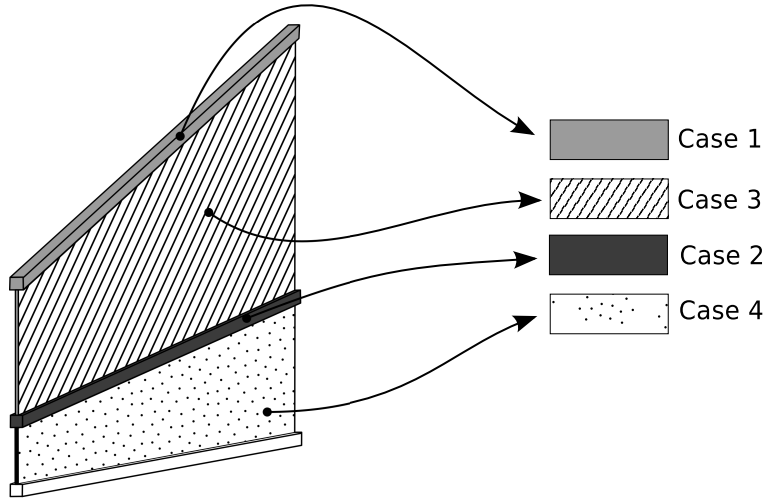


Figure 7: Damage at the component level: The considered cases.

	Undamaged		Case 1			Case 2			Case 3			Case 4	
	d=0	d=0.9	d=0.5	d=0.1	d=0.9	d=0.5	d=0.1	d=0.9	d=0.5	d=0.1	d=0.9	d=0.5	d=0.1
f_1	7.14	6.88	5.37	2.96	6.06	6.35	5.03	7.13	7.00	3.95	7.14	7.13	7.09
f_2	7.89	7.81	7.71	7.66	7.77	7.52	7.42	7.86	7.72	5.47	7.89	7.89	7.87
f_3	12.31	12.30	12.24	11.65	12.27	12.01	11.01	11.84	8.99	6.78	12.12	10.64	8.57
f_4	13.02	13.02	13.00	12.76	12.96	12.77	12.49	12.84	12.22	7.54	12.84	12.64	12.61
f_5	18.02	18.01	17.95	15.25	18.01	17.95	16.25	17.12	13.25	8.07	18.01	17.98	17.95
f_6	23.75	23.74	23.62	17.73	23.74	23.65	18.07	22.56	16.98	9.21	23.75	23.72	18.99
f_7	28.44	28.41	27.97	23.30	28.42	28.15	23.50	27.02	20.29	10.43	28.43	28.42	23.07
f_8	32.54	32.49	31.39	28.22	32.50	31.68	28.20	30.93	23.20	11.43	32.54	32.54	23.71
f_9	36.07	36.05	34.39	32.20	36.06	35.16	32.48	34.24	25.56	12.90	36.07	36.07	27.35
f_{10}	41.33	41.05	36.47	36.09	41.10	36.14	35.85	39.5	29.87	13.53	41.33	41.06	28.43
f_{11}	46.97	45.39	42.16	40.44	45.72	42.20	41.19	46.59	35.04	15.69	46.82	41.82	31.96
f_{12}	47.57	47.27	47.22	42.55	47.46	47.40	42.82	46.92	37.20	16.73	47.51	46.86	32.54
f_{13}	49.62	49.57	49.52	47.14	49.37	48.90	47.27	47.53	44.67	20.07	49.60	47.46	36.06
f_{14}	50.85	50.03	50.01	49.49	49.71	49.65	48.75	49.5	46.06	21.92	49.97	49.44	36.83
f_{15}	52.98	52.92	52.71	50.00	52.88	52.62	49.47	50.85	46.67	22.03	52.96	49.78	41.29

Table 2: First 15 frequencies of the 3-stringer composite panel for different damaged components.

257 The components that were considered damaged are: the upper stringer, case 1; the upper
 258 panel, case 3; the central stringer, case 2; and finally the bottom panel, case 4.

259 Table 2 reports the frequencies obtained from a free-vibration analysis in which the three
 260 values of damage, d , were applied for each damage configuration. The diagrams shown in Figure
 261 8 are used to show the variations in the frequencies at each damage level considering the four
 262 considered cases. Figure 9 shows the correlation factor, MAC, of the modal shapes for different
 263 damage levels.

264 Figure 8 shows the variations in the frequencies when the upper stringer is considered as the
 265 damaged component, that is, for the case 1. The results show that a damage magnitude $d = 0.9$

266 does not induce a large variation in the frequency values. When a damage level of $d = 0.5$ or
267 $d = 0.1$ is considered, a general reduction of the frequency values appears. Second, third and
268 fourth frequencies seem to be affected slightly by the damage, and this can be explained by
269 looking at the modal shapes in Figure 5. These modes show a notable deformation in the panel
270 area, that is, the damage to the stringer did not produce a strong variation of the response. The
271 correlation between the modal shapes of the undamaged and damaged structures can be observed
272 in Figures 9a, b and c . The MAC value shows that, when a low level of damage ($d = 0.9$) is
273 considered, only the higher modes present variations. Figure 9a shows that the modes 11 and
274 12 are not closely correlated to those of the intact structure. When the damage level becomes
275 larger, the modes at lower frequencies can also be affected, as shown in Figure 9b, where the 9th
276 mode is clearly not correlated to the modes of the damaged structure. At the maximum damage
277 level, $d = 0.1$, the first modes also show a small correlation value and they may present some
278 switch in the order in which they appear.

279 Case 2 introduces damage to the central stringer. The frequencies show a similar behavior
280 to those of the previous case, as can be seen in Figure 8. The modes at higher frequencies are
281 affected more for low values of damage, as shown in Figures 9d and 9e, while, for a high damage
282 level, the first modes also show a poor correlation to the undamaged structure, Figure 9f.

283 The last two cases introduce damage to the two panels. In these cases, the damage has a
284 great influence on the frequency values because it changes the shell-like modes of the panel, as
285 shown in Figure 8. A low damage level in the upper panel may produce a strong variation in
286 the higher frequencies, as shown in Figure 9g. An increase in the damage of this component
287 produces a drop in the frequency values and their modal shapes completely lose the correlation
288 with respect to the undamaged structure, as shown in Figures 9h and 9i.

289 The consequences of damage in the lower panel are not as severe as in the previous case,
290 Figures 9j and 9k, but when a high level of deterioration is considered, Figure 9l, several modes
291 of the damaged structure lose their correspondence with those of the intact structure.

292 3.3.2. Failure at the layer level

293 Figures 10a,b and c show the cases in which a single layer fails. In this case, refined models
294 that are able to provide a layer-wise description are mandatory to describe the damage accurately.
295 Table 3 shows the first 15 frequencies considering the three damage levels for each considered
296 case. As in the previous cases, the variations in the frequencies have been reported using the
297 histograms shown in Figure 11.

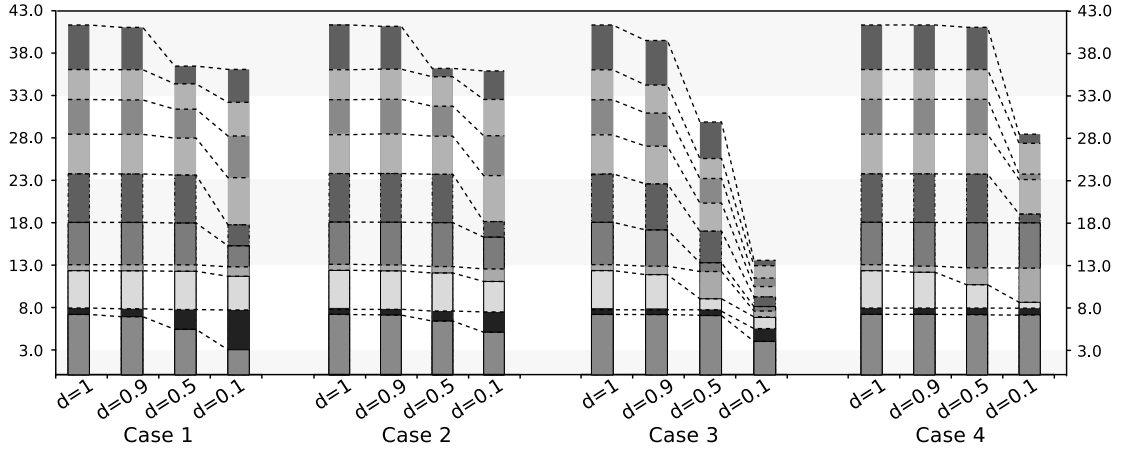


Figure 8: Frequency variations due to different damage conditions.

298 Cases 5a and 5b consider the failure of an external and an internal layer, respectively. The
 299 results reported in Figure 11 show that the failure of the external layer, case 5a, is more critical
 300 and produces a larger variation in the natural frequencies. The analysis of the MAC correla-
 301 tion, reported in Figure 12, points out that a reduction of 50% of the external panel integrity,
 302 Figure 12b, can have a remarkable effect on the higher modes, while 90% of failure, Figure 12c,
 303 completely changes the dynamic response of the structure. When an internal layer fails, more
 304 damage is required to change the modal shapes; in fact only when the properties of the panel are
 305 reduced by 90%, Figure 12e, is the correlation poor for higher modes. In both cases the first two
 306 modes and frequencies are not affected by the damage because they are governed by the stiffness
 307 of the stiffeners.

308 The third case considers the failure of the two external layers. Considering a damage level of
 309 $d = 0.9$, the frequencies are reduced slightly, but the higher modal shapes show some variations,
 310 as can be seen in the correlation reported in Figure 12g. The increase in the damage causes a
 311 drop in the frequency values and the modal correlation only shows values close to unity for few
 312 modes. When 90% of the layer properties have been lost, see Figure 12i, only the first mode can
 313 be compared with that of the intact structure.

314 3.3.3. Local damage

315 In this section, the damage has been considered localized in a small area of the upper panel
 316 of the structure. Figure 14a shows the 45 areas where the failure has been considered. A
 317 damage value of $d = 0.1$ was applied to all of the four layers of the considered area. Figure 13
 318 shows the variations in the first eight natural frequencies when the failure appears in one of the

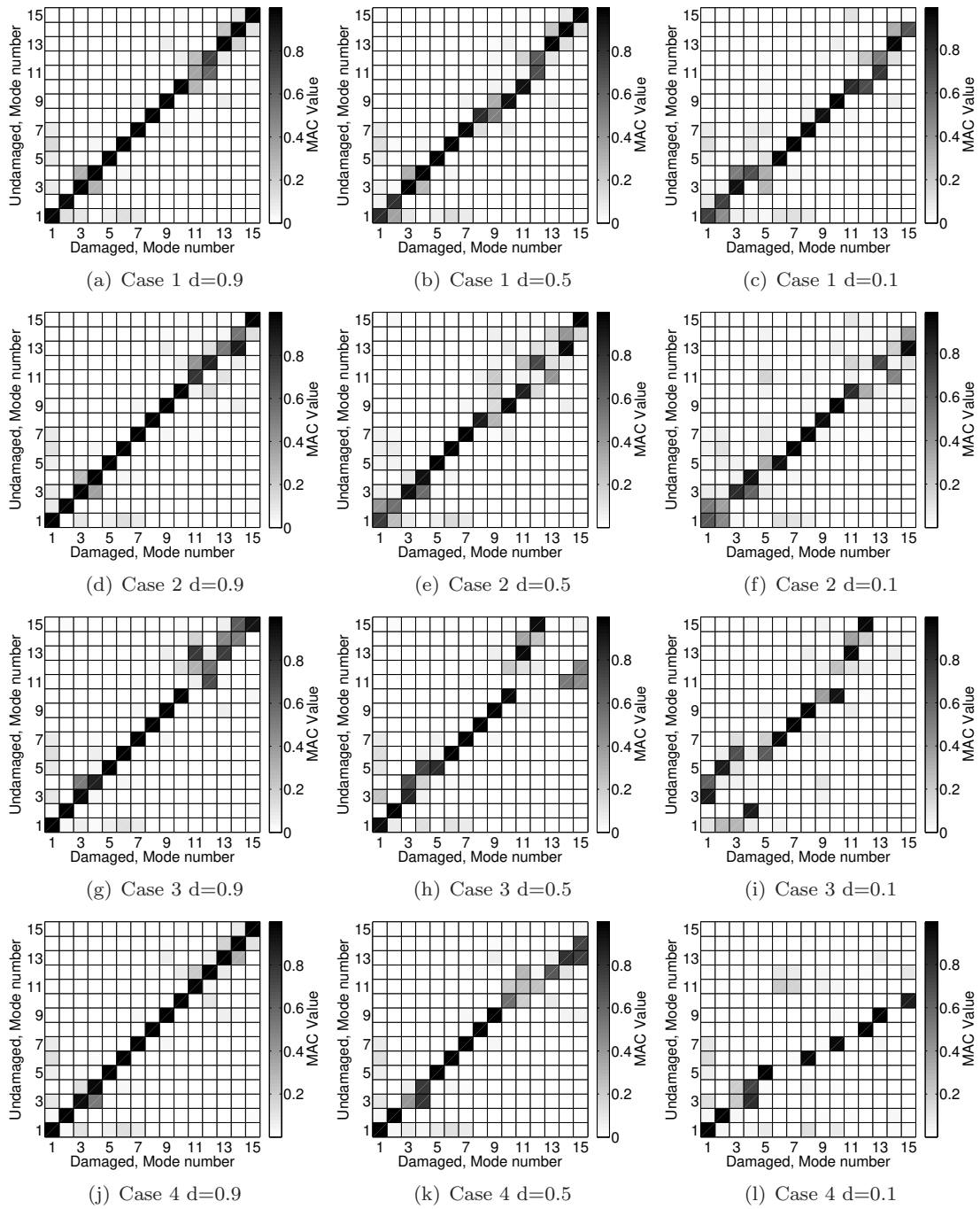


Figure 9: Correlation between the intact and the damaged structures.

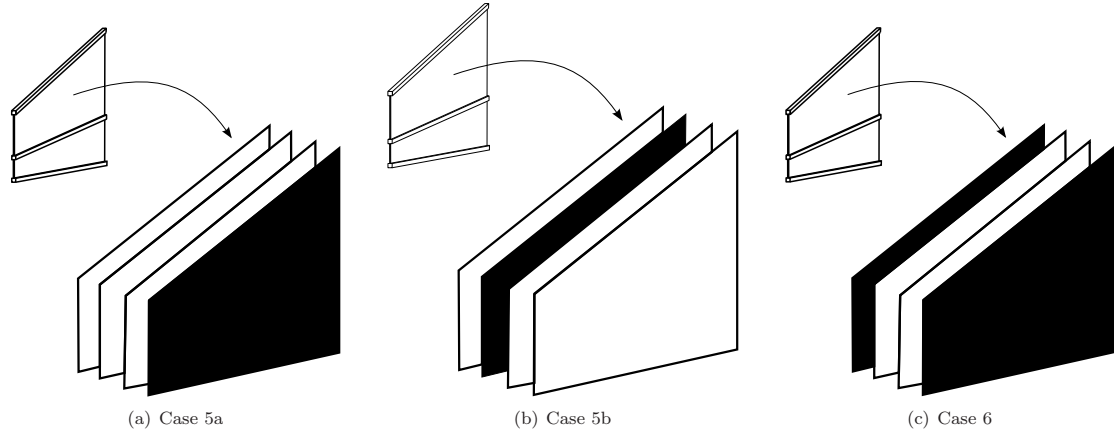


Figure 10: Damaged component cases.

	Undamaged		Case 5a		Case 5b		Case 6			
	d=0	d=0.9	d=0.5	d=0.1	d=0.9	d=0.5	d=0.1	d=0.9	d=0.5	d=0.1
f_1	7.14	7.14	7.12	7.09	7.14	7.13	7.10	7.14	7.09	6.93
f_2	7.89	7.88	7.84	7.79	7.88	7.85	7.80	7.87	7.79	7.70
f_3	12.31	12.17	11.29	9.83	12.24	11.85	11.15	12.01	10.22	7.73
f_4	13.02	12.94	12.75	12.51	12.98	12.85	12.75	12.88	12.61	10.16
f_5	18.02	17.69	16.10	13.66	17.89	17.28	16.34	17.37	14.50	12.37
f_6	23.75	23.32	21.15	17.49	23.59	22.77	21.47	22.89	18.92	13.33
f_7	28.44	27.93	25.51	21.57	28.23	27.23	25.75	27.44	22.96	16.14
f_8	32.54	32.02	29.58	24.99	32.26	30.87	28.73	31.50	26.77	18.90
f_9	36.07	35.29	31.34	26.28	35.92	35.20	34.16	34.54	27.67	20.67
f_{10}	41.33	40.71	37.56	31.17	41.06	39.66	37.40	40.09	33.95	21.84
f_{11}	46.97	46.92	42.31	32.79	46.95	46.85	46.06	46.77	36.89	25.37
f_{12}	47.57	47.33	45.87	39.48	47.49	47.11	46.73	47.74	41.74	27.60
f_{13}	49.62	48.59	46.83	41.45	49.48	48.75	47.54	47.02	46.65	30.30
f_{14}	50.85	49.87	48.16	46.65	49.99	49.76	48.74	49.70	47.21	35.21
f_{15}	52.98	52.14	50.19	46.67	52.64	51.08	50.05	51.39	49.75	35.67

Table 3: First 15 frequencies of the 3-stringer composite panel considering different failure cases at the layer level.

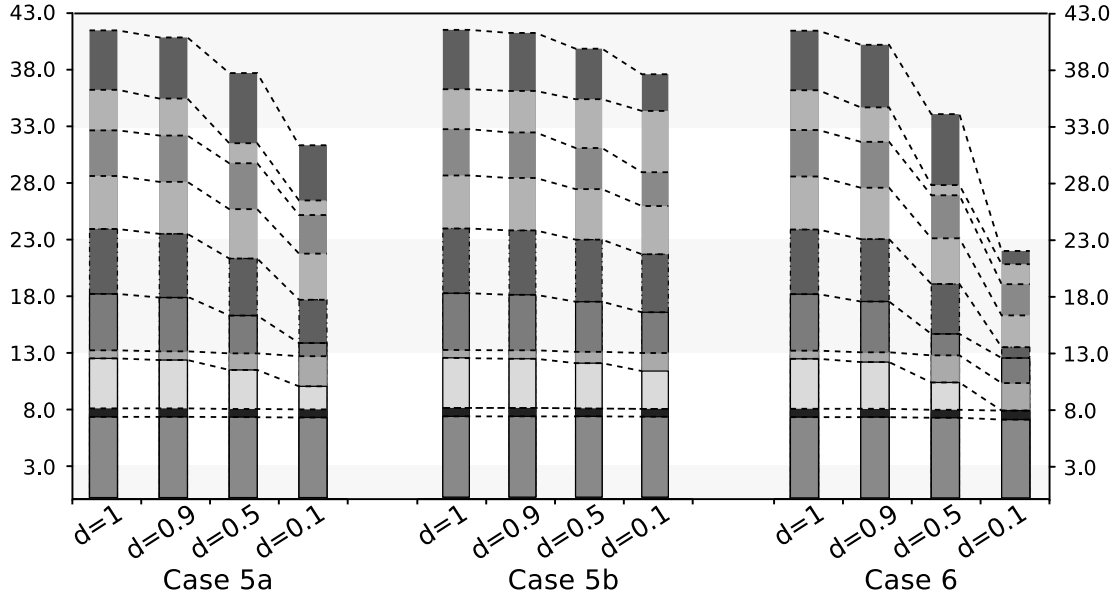


Figure 11: Frequency variation for different failure cases at the layer level.

319 45 considered areas. This histogram shows that local damage to the panel has only a limited
 320 influence on the first frequencies, but can affect the frequencies at higher values. The results
 321 highlight which areas of the panel are more sensitive to failure, e.g., failure in panels 11, 12 or
 322 13 has a greater impact on the eighth frequency that failure in area 6; on the other hand failure
 323 in panel 27 mainly involves the sixth frequency.

324 These results can be used to detect the position of damage from variations in the natural
 325 frequencies. The results have been elaborated in the colored maps reported in Figure 14. A map
 326 has been introduced for each natural frequency, in which the colors represent the variations in
 327 frequency values when failure is applied in that area. The darker the color is, the stronger the
 328 variation in the frequency value. The parameter, f^* , is reported in Equation 24.

$$f^* = \frac{f}{(f_d - f)_{max}} \left(\frac{f_d - f}{f} \right) \begin{cases} f_d = \text{damaged frequency} \\ f = \text{undamaged frequency} \end{cases} \quad (24)$$

329 A value equal to 1 (black color) denotes the area that produces the maximum decrease in fre-
 330 quency.

331 These maps can be used to locate damage from variations in the natural frequencies. If a
 332 drop in the first frequency appears, it is possible to presume that the failure is locate in area
 333 9, as shown in Figure 14b. According to the same approach, a variation in the third frequency

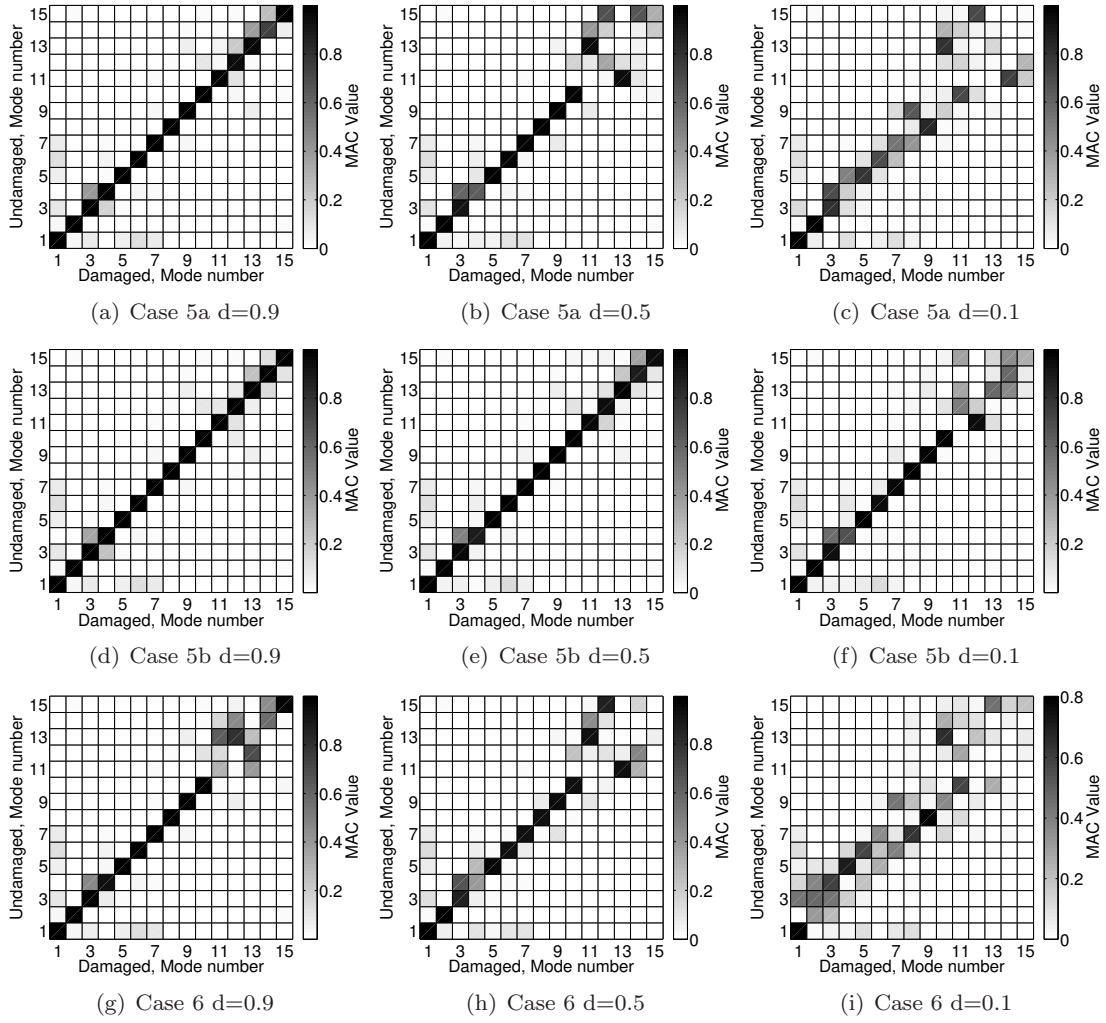


Figure 12: Correlation between the structures with intact and damaged panel layers.

334 suggests damage in area 21 or 22, see Figure 14d, while a reduction in the fifth frequency denotes
 335 failure in area 25.

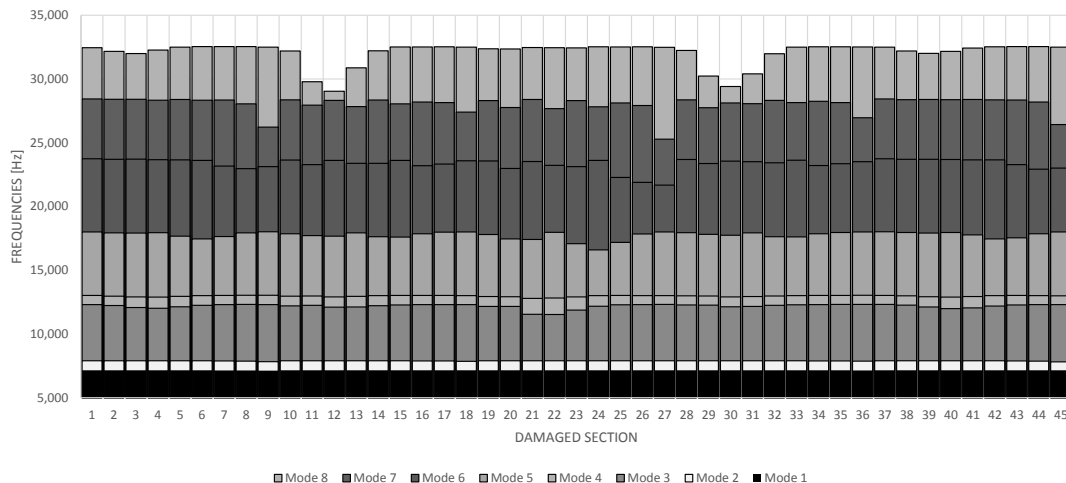
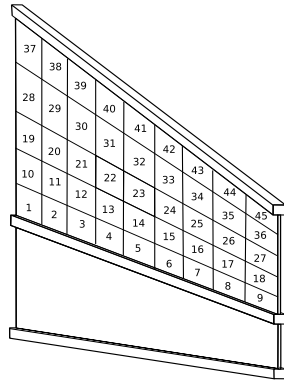


Figure 13: Variations in the first 8 frequencies for different local failures.

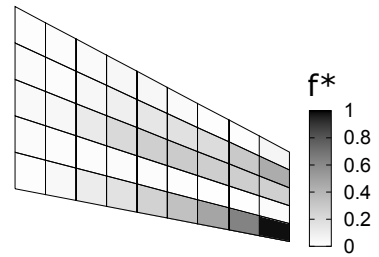
336 3.4. Wing-box structure

337 An example of a complex aeronautic structure is considered in this section. A multi-component
 338 tapered wing-box has been analyzed, Figure 15 shows its geometry. The wing has a length of
 339 $L = 5 \text{ m}$. The tapered shape modifies the chord which changes from a value of $R_1 = 1.48 \text{ m}$
 340 to a value of $R_2 = 0.782 \text{ m}$. The wing-box thickness is constant, and it is equal to $H = 0.208$
 341 m . The spar is composed of two spar caps and a spar web with a thickness of $t_w = 3 \text{ mm}$. The
 342 spar caps have dimensions equal to $a = 8 \text{ mm}$, $b = 5 \text{ mm}$, $c = 20 \text{ mm}$ and $d = 45 \text{ mm}$. The
 343 spars are made of aluminum alloy which has the same proprieties as the previously mentioned
 344 material. The skin is a 4-layer laminate made of CFRP, and it has a thickness of $t_s = 4 \text{ mm}$.
 345 The mechanical proprieties of the CFRP are equal to those used in the previous case. There are
 346 three ribs made of aluminum, which are placed at $Yr = 1,6666667 \text{ m}$. Their thickness is equal
 347 to t_s . The central spar is aligned with the Y_G -axis.

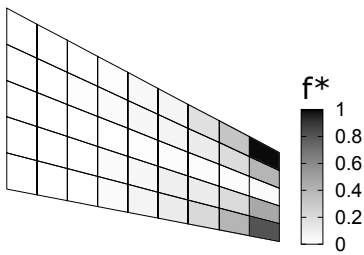
348 For the sake of brevity, only the effects of six different failures have been considered for the
 349 first bending and first torsional modes. A solid Nastran solid model, with more than 400000
 350 DOFs, was used for validation purposes. The LE model used six 4-node beam elements, along
 351 the length of the spar-caps and one 3-node beam element placed over the thickness to describe
 352 each web and each layer of the skin. The same layout was used for the ribs. Figure 16 shows



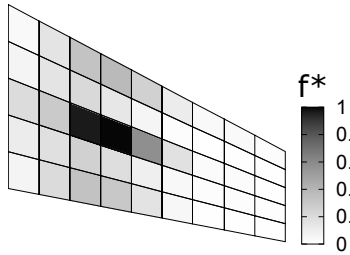
(a) Damaged area numbering



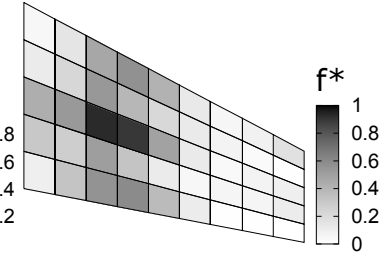
(b) Frequency 1



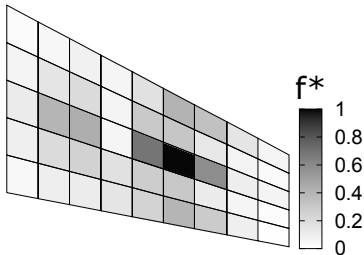
(c) Frequency 2



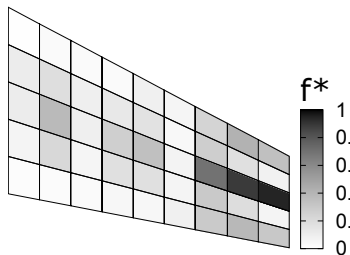
(d) Frequency 3



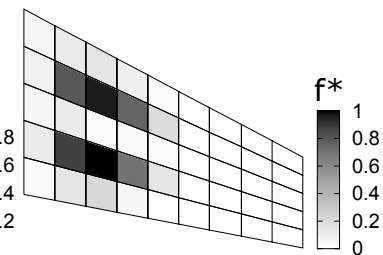
(e) Frequency 4



(f) Frequency 5



(g) Frequency 6



(h) Frequency 8

Figure 14: Damage influence maps. For each frequency the map shows the area which, if damaged, has the greatest effect on that frequency value.

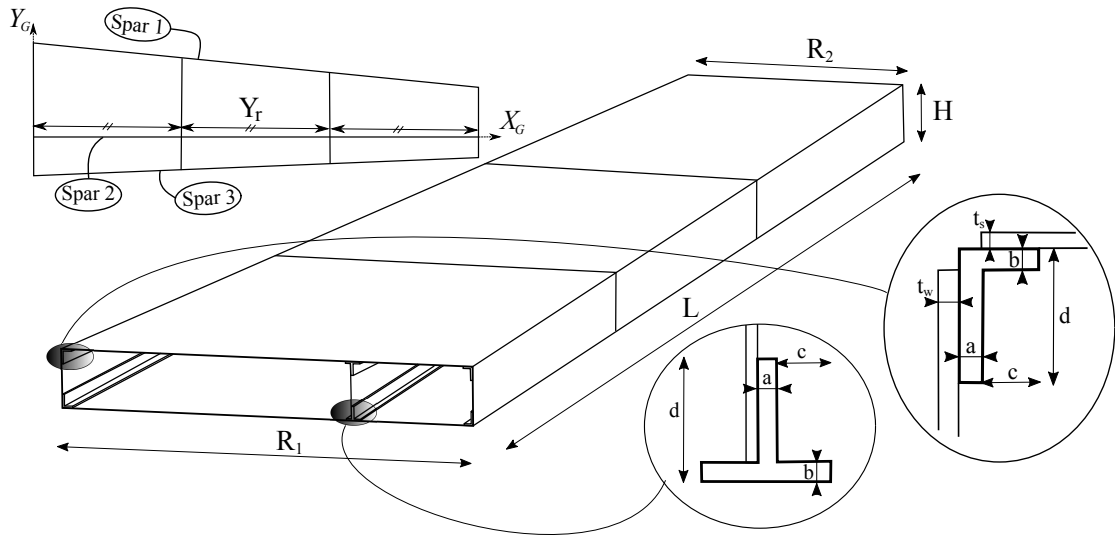


Figure 15: Considered wing structure.

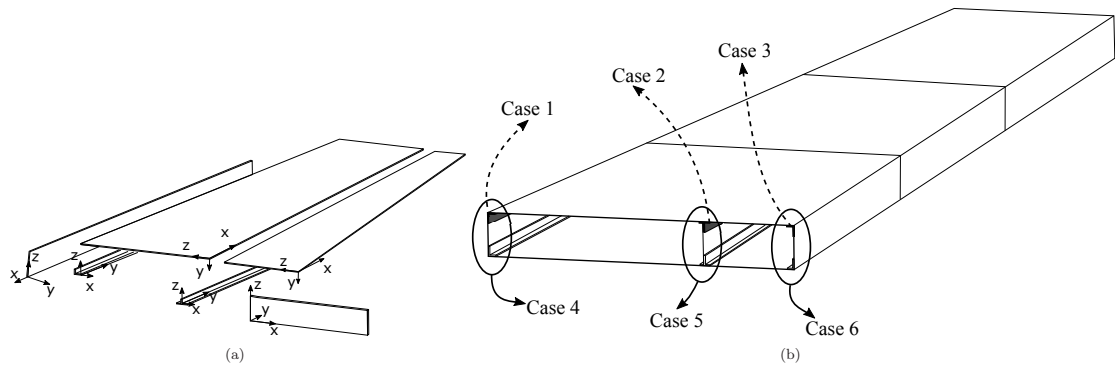


Figure 16: Local beam frames (a) and Damage cases (b)

	Solid	LE Model
DOFs	>400000	42468
1 st B	9.57	9.58
1 st T	38.54	39.40

Table 4: Assessment of the present model. First bending mode, 1st B. First torsional mode, 1st T.

	Undamaged	Top Spar Caps failure			Complete Spar failure		
		Case 1	Case 2	Case 3	Case 4	Case 5	Case 6
1 st B	9.58	9.35	9.30	9.35	8.96	8.87	9.01
1 st T	39.40	38.91	39.15	39.18	35.70	37.73	37.67

Table 5: Different Conditions of damaged spars with a damage level of $d = 0.1$.

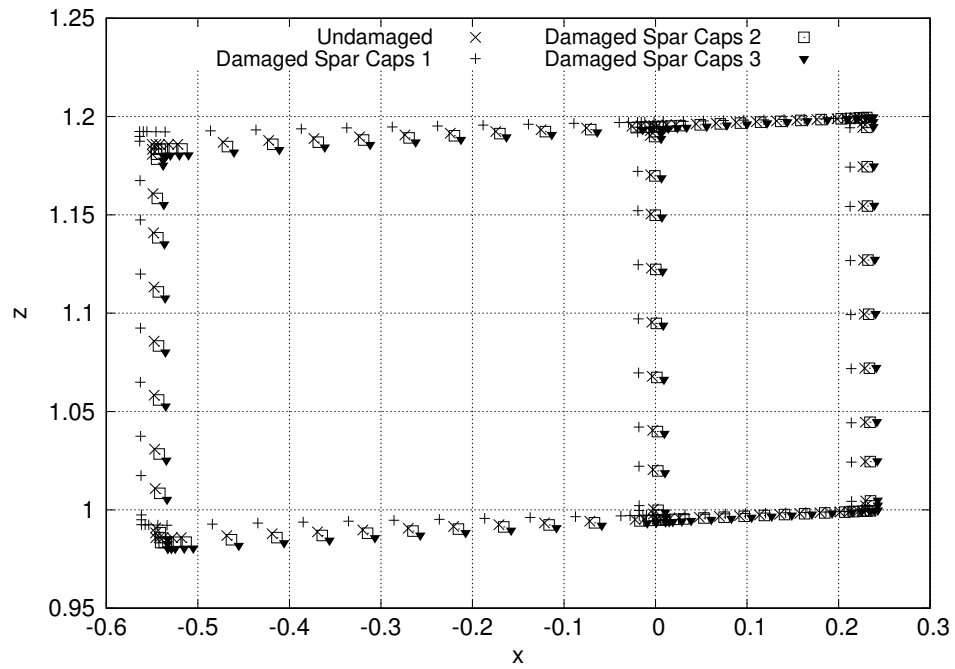
the orientation of the local frame for each component, where y identifies the beam axis. The model has 42468 DOFs. Table 4 shows the results obtained using the present model and the solid model built using the commercial Nastran code. The results show the accuracy of the present model, even when complex structures are considered. Moreover, the LE Model provides accurate results, but only uses a fraction of the DOFs required by the Solid model which, in order to respect the geometrical aspect ratio limitation, requires a huge number of elements for the analysis of thin-walled structures.

The first three damaged configurations, cases 1 to 3, only consider the failure of the top caps of each spar. Cases 4 to 6 consider the complete failure of the spar, that is, both the caps and web were considered damaged. All six cases consider a damage parameter, d , equal to 0.1.

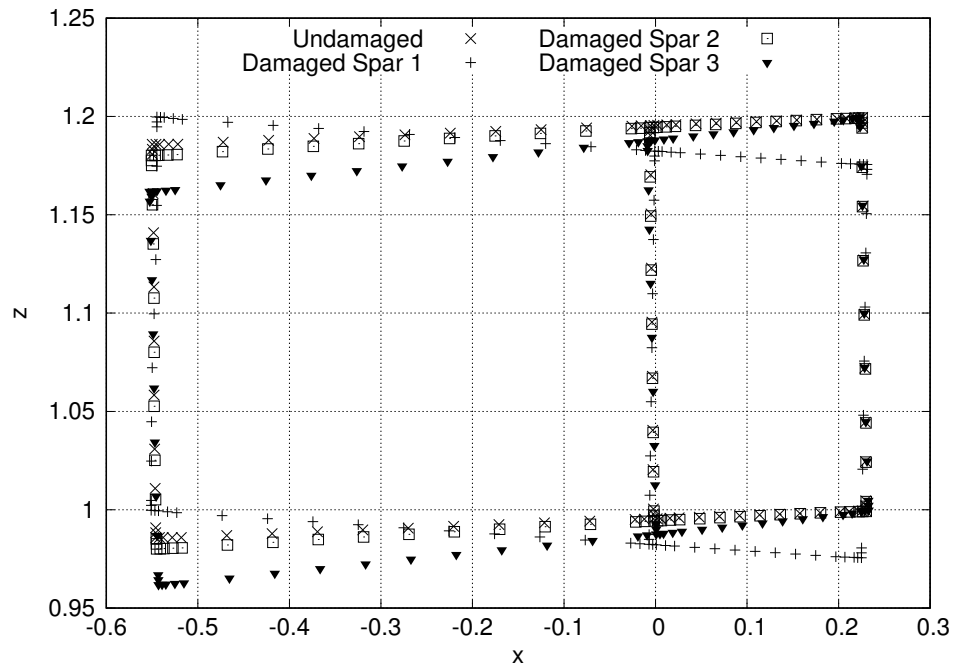
Table 5 shows the frequencies obtained from the analyses of the six configurations. The first bending frequency is almost unaffected by the failure of the caps but it shows a decrease when the frontal and the central spars are damaged. The failure of the central spar, case 5, produces a drop in the first bending frequency of 7.4%.

An analysis of the modal shapes shows more details about the effects of the failure. Figure 17a presents the modal shapes of the first bending mode, considering the tip section of the wing. The damage located in the caps of the first spar reduces the torsional effect due to the tapered shape. On the other hand, case 3 increases this effect. The effects of the damage on the whole spar are more significant, as shown in Figure 17b. In this case, it can be observed that the failure of the first spar changes the torsion angle. This could be of great interest when coupling phenomena are present, e.g., in aero-elastic phenomena.

As expected, when the first torsional mode is considered, the critical component is the first

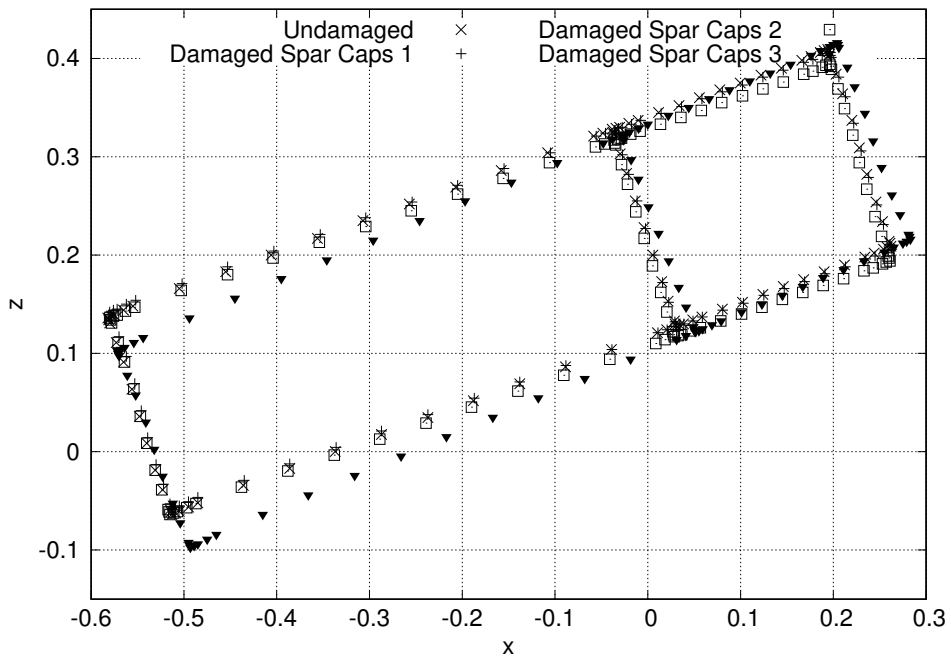


(a) Failure of the spar cap

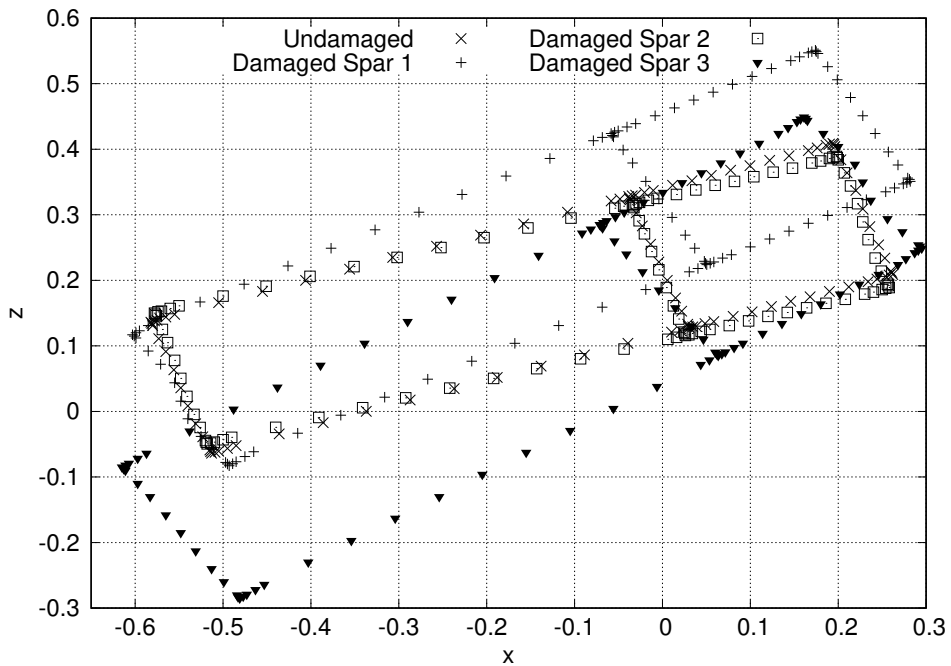


(b) Failure of the whole spar

Figure 17: Influence of damage on the 1st bending mode.



(a) Failure of the spar cap



(b) Failure of the whole spar

Figure 18: Influence of damage on the 1st torsional mode.

375 spar. The failure of this element produces a strong reduction in the torsional stiffness, because of
376 the reduction in the strength of the frontal closed cell. The Case 4 failure introduces a decrease
377 of 9.4% in the frequency value. Figure 18 shows the effects on the modal shape at the tip of the
378 wing. The damage of the whole spar introduces sensible effects, particularly for case 4 and case
379 6.

380 4. Final Remarks

381 In this work, the capabilities of an advanced one-dimension model have been exploited to
382 study the dynamic response of damaged composite structures. This model introduces a three-
383 dimensional description of the structure with no geometrical approximations and a deformable
384 cross-section of the beam. These features allow a quasi-3D solution to be obtained and make
385 the models able to deal with non-classical and local effects due to global and local failure of a
386 complex composite structure. The failure of the structure has been considered by introducing
387 degradation of the material properties, thus the stiffness in the damaged area is reduced. The
388 present model has been used to study the variations in the natural frequencies of a structure that
389 has suffered from the failure of a single component, the failure of one or more layers or the failure
390 of a small area of a panel. The Modal Assurance Criteria, MAC, has been used to evaluate the
391 variations in the modal shapes. The following remarks can be made concerning the results:

- 392 • In all the considered cases the present model has been able to accurately predict the natural
393 frequencies and the modal shapes, with a reduction in the computational costs, compared
394 with solid models.
- 395 • The component-wise approach allows the failure of a single component to be introduced.
- 396 • The layer-wise model used in the present work makes it possible to consider the damage
397 of each single layer, and thus to evaluate the consequences on the natural frequencies and
398 modal shapes.
- 399 • The analysis of a local failure and the derivation of a database of possible scenarios could
400 lead to the fast detection of failure on the basis of variations in the natural frequency.
- 401 • The present approach can easily be extended to complex structures, such as wing boxes.

402 In short, thanks to its efficiency and accuracy, the present model can be used to characterize the
403 behavior of complex structures when they suffer from failure at different levels. The present re-

404 sults could be used to derive future approaches for the health monitoring of composite structures
405 or their maintenance procedure.

406 References

- 407 [1] Z. Zhang, K. Shankar, E. Morozov, M. Tahtali, Vibration-based delamination detection in
408 composite beams through frequency changes, *Journal of Vibration and Control* 22 (2) (2016)
409 496–512. doi:10.1177/1077546314533584.
- 410 [2] R. Capozuzza, Vibration of cfrp cantilever beam with damage., *Composite Structures* 116
411 (2014) 211–222.
- 412 [3] Y. Wang, M. Liang, J. Xiang, Damage detection method for wind turbine blades based on
413 dynamics analysis and mode shape difference curvature information., *Mechanical Systems
414 and Signal Processing* 48 (2014) 351–367.
- 415 [4] K. Nguyen, Mode shapes analysis of a cracked beam and its application for crack detection.,
416 *Journal of Sound and Vibration* 333 (3) (2014) 848–872.
- 417 [5] H. Pollayi, W. Yu, Modeling matrix cracking in composite rotor blades within vabs frame-
418 work., *Composite Structures* 110 (2014) 62–76. doi:10.1016/j.compstruct.2013.11.012.
- 419 [6] M. Perez, L. Gil, M. Sánchez, , S. Oller, Comparative experimental analysis of the effect
420 caused by artificial and real induced damage in composite laminates., *Composite Structures*
421 112 (2014) 169–178.
- 422 [7] L. Euler, *De curvis elasticis. Methodus inveniendi lineas curvas maximi minimive proprietate*
423 *gaudentes, sive solutio problematis iso-perimetrici lattissimo sensu accepti.*
- 424 [8] S. Timoshenko, J. Goodier, *Theory of elasticity*, McGraw-Hill, 1970.
- 425 [9] P. Cicala, *Sulle travi di altezza variabile*, Laboratorio di Aeronautica, Tipografia Vincenzo
426 Bona, Turin, Italy, 1939.
- 427 [10] D. Just, Plane frameworks of tapering box and I-section, *Journal of the Structural Division*
428 103 (1) (1977) 71–86.
- 429 [11] C. Brown, Approximate stiffness matrix for tapered beams, *Journal of Structural Engineer-*
430 *ing* 110 (12) (1984) 3050–3055. doi:10.1061/(ASCE)0733-9445(1984)110:12(3050).

- 431 [12] H. Schreyer, Elementary theory in linearly tapered beams, *Journal of the Engineering Me-*
432 *chanics Division* 104 (3) (1978) 515–527.
- 433 [13] E. Carrera, A. Pagani, M. Petrolo, Component-wise method applied to vibration
434 of wing structures., *Journal of Applied Mechanics* 80 (4) (2013) Paper 041012.
435 doi:10.1115/1.4007849.
- 436 [14] E. Carrera, A. Pagani, Accurate response of wing structures to free-vibration, load factors,
437 and nonstructural masses., *AIAA Journal* 54 (1) (2016) 227–241.
- 438 [15] E. Zappino, E. Carrera, Multidimensional model for the stress analysis of reinforced shell
439 structure, *AIAA Journal*In Press. doi:10.2514/1.J056384.
- 440 [16] E. Carrera, E. Zappino, T. Cavallo, Accurate free vibration analysis of launcher structures
441 using refined 1d models, *International Journal of Aeronautical and Space Sciences* 16 (2)
442 (2015) 206–222. doi:10.5139/IJASS.2015.16.2.206.
- 443 [17] E. Carrera, A. Pagani, M. Petrolo, Free vibrations of damaged aircraft struc-
444 turesby component-wise analysis., *AIAA JOURNAL* 54 (10) (2016) 3091–3106.
445 doi:10.2514/1.J054640.
- 446 [18] R. Allemang, D. Brown, A correlation coefficient for modal vector analysis., *Proceedings of*
447 *the International Modal Analysis Conference* (1982) 110–116.
- 448 [19] O. Salawu, C. Williams, Bridge assessment using forcedvibration testing., *Journal of Struc-*
449 *tural Engineering* 121 (2) (1995) 161–173.
- 450 [20] E. Zappino, A. Viglietti, E. Carrera, The analysis of tapered structures using a component-
451 wise approach based on refined one-dimensional models., *Aerospace Science and Technology*
452 65 (2017) 141–156.
- 453 [21] E. Zappino, A. Viglietti, E. Carrera, Analysis of tapered composite structures using a refined
454 beam theory., *Composite Structures* 183 (2017) 42–52.
- 455 [22] E. Carrera, C. M., M. Petrolo, E. Zappino, *Finite Element Analysis of Structures Through*
456 *Unified Formulation*, John Wiley & Sons, 2014.
- 457 [23] S. Tsai, *Composites Design*, 4th Edition, Dayton, Think Composites, 1988.

- 458 [24] J. Reddy, Mechanics of laminated composite plates and shells. Theory and Analysis, 2nd
459 Edition, CRC Press, 2004.
- 460 [25] E. Carrera, G. Giunta, M. Petrolo, Beam Structures: Classical and Advanced Theories,
461 Wiley, Hoboken, 2011.
- 462 [26] E. Carrera, A. Pagani, M. Petrolo, Classical, refined, and component-wise analysis of
463 reinforced-shell wing structures., *AIAA JOURNAL* 51 (5) (2013) 1255–1268.
- 464 [27] E. Carrera, M. Petrolo, Refined Beam Elements With Only Displacement Variables and
465 Plate/Shell Capabilities., *Meccanica* 47 (3) (2012) 537–556.
- 466 [28] E. Carrera, E. Zappino, Carrera Unified Formulation for Free-Vibration Analysis of Aircraft
467 Structures., *AIAA Journal* 1 (54) (2016) 280–292.
- 468 [29] T. Cavallo, E. Zappino, E. Carrera, Component-wise vibration analysis of stiffened plates
469 accounting for stiffener modes., *CEAS Aeronautical Journal* 8 (2) (2017) 385–412.